激光与光电子学进展 先进成像

Three-Dimensional Shape Measuring Method Based on Dual-Frequency Digital Moiré Fringe

Hu Hailing[1,3,5], He Renji[1,3], Chen Yang[1,3,5], Zhang Peiqing[2,3,5], Shen Xiang[2,3,4,5], Da Shixun[2,3,5], Song Baoan[1,3,5*]

[1]*Faculty of Electrical Engineering and Computer Science, Ningbo University, Ningbo* 315211, *Zhejiang, China*;
[2]*The Research Institute of Advanced Technologies, Ningbo University, Ningbo* 315211, *Zhejiang, China*;
[3]*Key Laboratory of Photoelectric Detecting Materials and Devices of Zhejiang Province, Ningbo* 315211, *Zhejiang, China*;
[4]*Ningbo Institute of Oceanography, Ningbo University, Ningbo* 315211, *Zhejiang, China*;
[5]*Engineering Research Center for Advanced Infrared Photoelectric Materials and Devices of Zhejiang Province, Ningbo* 315211, *Zhejiang, China*

Abstract A dual-frequency digital Moiré measurement method (DFDM) is proposed for the three-dimensional (3D) shape measurement of an object. The high- and low-frequency fringes are modulated separately along orthogonal direction using different carrier frequencies before being projected onto the measured object. After collecting and demodulating the composite fringe, the digital π phase shift is used to remove the DC component of the demodulated fringes, resulting in high-precision Moiré fringes for calculating the wrapped phase. The unwrapping of the high-frequency wrapped phase is guided by the low-frequency phase to further realistically reconstruct the surface of the measured object. When compared with existing single-shot digital Moiré profilometry, DFDM effectively removes the DC component of the fringe and calculates the phase more accurately.

Key words 3D measurement; dual-frequency; digital Moiré fringe; digital π phase shift

中图分类号 O43 **文献标志码** A **DOI**: 10.3788/LOP222658

1 Introduction

Optical three-dimensional (3D) measurement technology[1-4] has the advantages of noncontact, fast measurement, and high precision. It is widely used in a variety of industries, including manufacturing, biomedical systems, computer science, and archaeological exploration. With the development of on-line detection and dynamic profilometry, real-time 3D measurement has become a research hotspot[5-8].

Because only one fringe is projected, Fourier transform profilometry (FTP) is the most common and simplest real-time 3D measurement method[9-12]. However, the aliasing of the zero frequency component and the fundamental frequency component in filtering would limit the measurement accuracy. Phase shift profilometry (PSP)[13] has high measurement accuracy, but it cannot be effectively used for real-time measurement due to the need to project multiple fringe patterns. Several improved methods for using PSP for real-time measurement have been proposed by researchers. Among these is a color phase-shift technology[14-17] that combines three fixed phase-shift fringes into the R, G, and B channels to achieve a three-step phase shift profile measurement. However, it does suffer from color coupling due to spectral overlap between adjacent channels, which is easily disturbed via the color of the object surface, and it is prone to introducing unavoidable errors in the measurement process. An orthogonal composite fringe method was developed[18]. Each phase-shift sinusoidal fringe was modulated via different frequency sinusoidal carriers

收稿日期: 2022-09-30; **修回日期**: 2022-10-06; **录用日期**: 2022-10-24; **网络首发日期**: 2022-11-04
基金项目: 国家自然科学基金(62075109, 62135011)、宁波大学王宽诚幸福基金
通信作者: *songbaoan@nbu.edu.cn

before being combined to form a composite fringe. More than three fringes were combined, and 256 gray levels were shared, with each fringe having a smaller grayscale range, resulting in low measurement accuracy and range in this method. In recent years, the digital Moiré technology has been proposed[19-21], which integrates the features of FTP and PSP, with high speed and high precision. Li et al. proposed a computer-generated Moiré profilometry (CGMP)[22] that collected only one deformed fringe, superimposed reference fringes, and deformed fringes with only AC components to synthesize the corresponding Moiré fringe. The wrapped phase was then calculated using the Moiré fringe. However, in the actual measurement process, the AC and DC components of the deformed fringe easily overlap in the frequency domain, making effective filtering of the DC component impossible and affecting the accuracy of CGMP. Wang et al. proposed an orthogonal modulation CGMP (OMCGMP)[23] to resolve spectrum aliasing which combined two sinusoidal fringes with a fixed phase shift of π. The DC component was removed by subtracting the two fringes demodulated from the captured composite deformed fringe. It effectively removes the DC component, but it only uses one frequency fringe to calculate the phase, limiting measurement accuracy, particularly when measuring objects with discontinuous surfaces.

A dual-frequency digital Moiré measurement method (DFDM) is proposed in this study to achieve rapid measurement of the object profile. While the DC component of the fringe is removed effectively, the measurement accuracy is improved using DFDM compared with the OMCGMP. This method's measurement principle is clarified, and its measurement accuracy is simulated and demonstrated. Finally, the 3D shape of discontinuous objects such as a face mask is measured experimentally, and the method's measurement accuracy is analyzed and compared.

2 Principle of DFDM

As shown in Fig. 1, two sinusoidal fringe patterns of high and low frequency are orthogonally modulated with two carrier fringe patterns of different frequencies, and then added together to form a composite fringe. To begin, the collected reference fringe can be expressed by projecting the composite fringe onto the reference plane:

$$I^R(x,y)=R(x,y)\left[C+D\sum_{n=1}^{2}\cos(2\pi F_n x)I_n^R(x,y)\right],\quad n=1,2, \tag{1}$$

where

$$I_n^R(x,y)=A+B\cos\left[2\pi f_n y+\varphi_{n0}(x,y)\right],\ n=1,2, \tag{2}$$

$R(x,y)$ represents the reflectivity of the reference plane; C and A represent the DC component of composite fringe and sinusoidal fringe, respectively; D and B represent the fringe contrast of composite fringe and sinusoidal fringe, respectively; F_n represents the carrier frequency and $F_1<F_2$; f_n represents the spatial frequency of sinusoidal fringe and $f_2=mf_1$ (m is a positive integer); $\varphi_{n0}(x,y)$ represents the phase value caused by the reference plane.

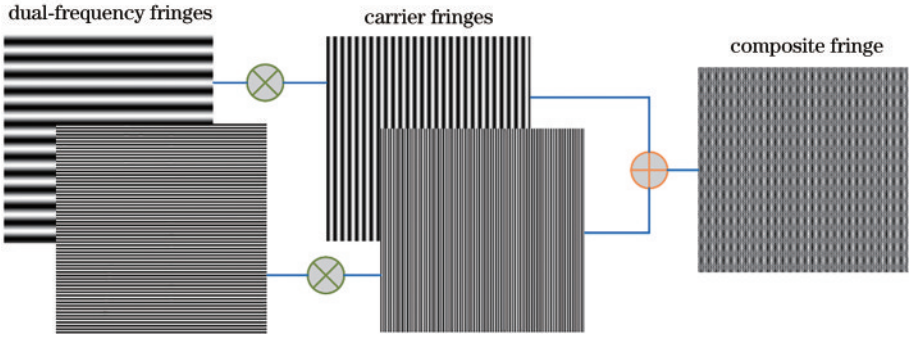

Fig. 1 Principle of fringe compounding

We demodulate Eq. (1) to obtain Eq. (3)[24]. If the demodulated single-frequency sinusoidal fringe still contains noise, the Butterworth filter is used to remove the noise's influence on the subsequent calculation.

$$I_n^{R0}(x,y)=\frac{1}{2}R(x,y)DA+\frac{1}{2}R(x,y)DB\cos\left[2\pi f_n y+\varphi_{n0}(x,y)\right],\ n=1,2。 \tag{3}$$

The most common method for removing the DC component in Eq. (3) is to use frequency domain high-pass filtering. However, this method is not applicable when the AC and DC components of the fringe are aliased. To remove the DC component of the fringe, the digital π phase shift method is proposed. First, we locate the troughs of the fringe according to $I_n^{R0}(x,y_i)<I_n^{R0}(x,y_{i-1})$ and $I_n^{R0}(x,y_i)<I_n^{R0}(x,y_{i+1})$, and use $I_n^{R0}(x,y_j)>I_n^{R0}(x,y_{j-1})$ and $I_n^{R0}(x,y_j)>I_n^{R0}(x,y_{j+1})$ to locate the peaks of the fringe, as shown via the red points in Fig. 2(a). Then, the median points are calculated using $\frac{I_n^{R0}(x,y_i)+I_n^{R0}(x,y_j)}{2}$. Because the fringe is discretized, the calculated median points may not be found on the fringe; instead, we find points near the calculated values [the initial points in Fig. 2(a)] and define these points as the initial median points. To find the median points with subpixel accuracy, the Akima interpolation method[25] is used. On the given interval $[y_i,y_{i+1}]$, if the function values I_i and I_{i+1} at the two endpoints and their derivatives I_i' and I_{i+1}' exist, then there is a continuous function value $I(y)$ in the given interval.

$$I(y)=a+b(y-y_i)+c(y-y_i)^2+d(y-y_i)^3, \tag{4}$$

where

$$\begin{cases} a=I_i \\ b=t_i \\ c=[\,3(I_{i+1}-I_i)/(y_{i+1}-y_i)-2t_i-2t_{i+1}\,]/(y_{i+1}-y_i) \\ d=[\,t_i+t_{i+1}-2(I_{i+1}-I_i)/(y_{i+1}-y_i)\,]/(y_{i+1}-y_i)^2 \end{cases}, \tag{5}$$

where t_i and t_{i+1} are the slopes at y_i and y_{i+1}, respectively, and $I(y)$ is the fringe intensity value with subpixel accuracy. Using Eqs. (4) and (5), interpolation is performed in the range of two points on the left and right sides of the initial median point, and the nearest point to the initial median point is found from the interpolated points to be the exact median point [the exact median points in Fig. 2(a)]. Lastly, using linear interpolation, these exact median points are used to create the center line, and a symmetric transformation is performed about the center line for $I_n^{R0}(x,y)$, as shown in Fig. 2(b), we can get

$$I_n^{R\pi}(x,y)=\frac{1}{2}R(x,y)DA+\frac{1}{2}R(x,y)DB\cos\left[2\pi f_n y+\varphi_{n0}(x,y)+\pi\right], \tag{6}$$

Eqs. (3) and (6) are subtracted to obtain the AC component of reference fringe $\tilde{I}_n^{R0}(x,y)$, as shown in Fig. 2(b):

$$\tilde{I}_n^{R0}(x,y)=I_n^{R0}(x,y)-I_n^{R\pi}(x,y)=R(x,y)DB\cos\left[2\pi f_n y+\varphi_{n0}(x,y)\right]. \tag{7}$$

Eq. (7) is transformed using the Hilbert transformation principle to obtain

$$\tilde{I}_n^{R\frac{\pi}{2}}(x,y)=R(x,y)DB\cos\left[2\pi f_n y+\varphi_{n0}(x,y)+\frac{\pi}{2}\right], \tag{8}$$

the obtained AC component fringe patterns, $\tilde{I}_n^{R0}(x,y)$ and $\tilde{I}_n^{R\frac{\pi}{2}}(x,y)$, are stored in the computer.

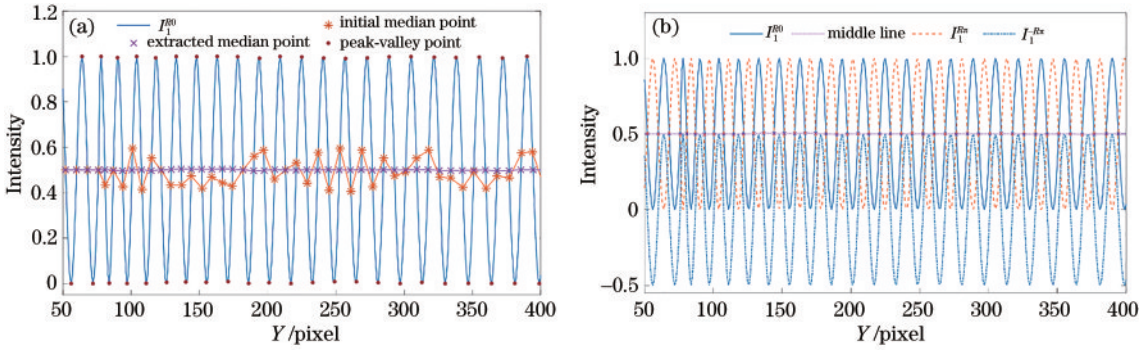

Fig. 2　Principle of digital π phase shift. (a) Median points before and after interpolation; (b) symmetry transform and remove DC component

The composite fringe is then projected onto the measured object, and the deformed composite fringe is collected:

$$I^O(x,y)=R'(x,y)\left[C+D\sum_{n=1}^{2}\cos(2\pi F_n x)I_n^O(x,y)\right],\quad n=1,2, \tag{9}$$

where

$$I_n^O(x,y)=A+B\cos\left[2\pi f_n y+\varphi_n(x,y)\right],\ n=1,2, \tag{10}$$

$R'(x,y)$ represents the reflectivity of the object surface; $\varphi_n(x,y)$ represents the phase value caused by the reference plane and the height of the object. We demodulate Eq. (9) and then use the digital π phase shift to remove the DC from the demodulated fringe.

The AC component of the deformed fringe obtained can be expressed as

$$\tilde{I}_n^{O0}(x,y)=R'(x,y)DB\cos\left[2\pi f_n y+\varphi_n(x,y)\right],\quad(11)$$

Moiré fringes are calculated using $\tilde{I}_n^{R0}(x,y)$, $\tilde{I}_n^{R\frac{\pi}{2}}(x,y)$, and $\tilde{I}_n^{O0}(x,y)$[22]:

$$I_n^{\text{Moire}0}(x,y)=\frac{1}{2}R(x,y)R'(x,y)B^2D^2\cos\left[\varphi_n(x,y)-\varphi_{n0}(x,y)\right],\ n=1,2,\quad(12)$$

$$I_n^{\text{Moire}\frac{\pi}{2}}(x,y)=\frac{1}{2}R(x,y)R'(x,y)B^2D^2\sin\left[\varphi_n(x,y)-\varphi_{n0}(x,y)\right],\ n=1,2,\quad(13)$$

the ratios of Eqs. (12) and (13) are just the tangent of the modulated phase, and they can be expressed as

$$\varphi_n(x,y)-\varphi_{n0}(x,y)=\arctan\frac{I_n^{\text{Moire}\frac{\pi}{2}}}{I_n^{\text{Moire}0}},\quad(14)$$

where $\varphi_n(x,y)-\varphi_{n0}(x,y)$ is calculated from the arctangent function, and its range is from $-\pi$ to π, thus a phase unwrapping algorithm is required to obtain a continuous phase. Let $\varphi_L(x,y)=\varphi_1(x,y)-\varphi_{10}(x,y)$ the low-frequency wrapping phase be indicated, $\varphi_H(x,y)=\varphi_2(x,y)-\varphi_{20}(x,y)$ and the high-frequency wrapping phase be indicated. $\varphi_L(x,y)$ can use the spatial approach to obtain a continuous phase $\phi_L(x,y)$. Eq. (15)[26-27] can be used to calculate the high-frequency unwrapped phase.

$$\phi_H(x,y)=2\pi\cdot\text{INT}\left[\frac{m\phi_L(x,y)-\varphi_H(x,y)}{2\pi}\right]+\varphi_H(x,y),\quad(15)$$

where INT(•) is the unsigned rounding operator and $m=f_2/f_1$. The phase-to-height relationship[28] shown in Eq. (16) can be used to calculate 3D reconstruction.

$$\frac{1}{h(x,y)}=a_1(x,y)+a_2(x,y)\frac{1}{\phi_h(x,y)}+a_3(x,y)\frac{1}{\phi_h(x,y)^2},\quad(16)$$

where $h(x,y)$ represents the height of the measured object and $a_1(x,y)$, $a_2(x,y)$, and $a_3(x,y)$ are system parameters obtained via calibration.

3 Simulation and analysis

The simulation generated a "crown ball" with a height of 60 mm, as shown in Fig. 3(a). The modulation frequencies of the two sinusoidal fringes are $f_1=1/16$ pixel and $f_2=1/4$ pixel, the two carrier frequencies are $F_1=1/12$ pixel and $F_2=1/4$ pixel. Fig. 3(b) is the deformed fringe of the DFDM, and the image size is 512 pixel × 512 pixel. Fig. 3(c) shows the corresponding spectrum distribution. Fig. 3(d) and Fig. 3(e) show low- and high-frequency sinusoidal fringes extracted from the composite deformed fringe, respectively using Filters 1 and 2. The digital π phase shift is used to remove the DC component of the fringe shown in Figs. 3(d) and 3(e) to generate high-precision Moiré fringe. Figs. 3(f) and 3(g) are two high-frequency digital Moiré fringe patterns with a phase difference of π/2 generated via calculation, respectively. The reconstructed result of the "crown

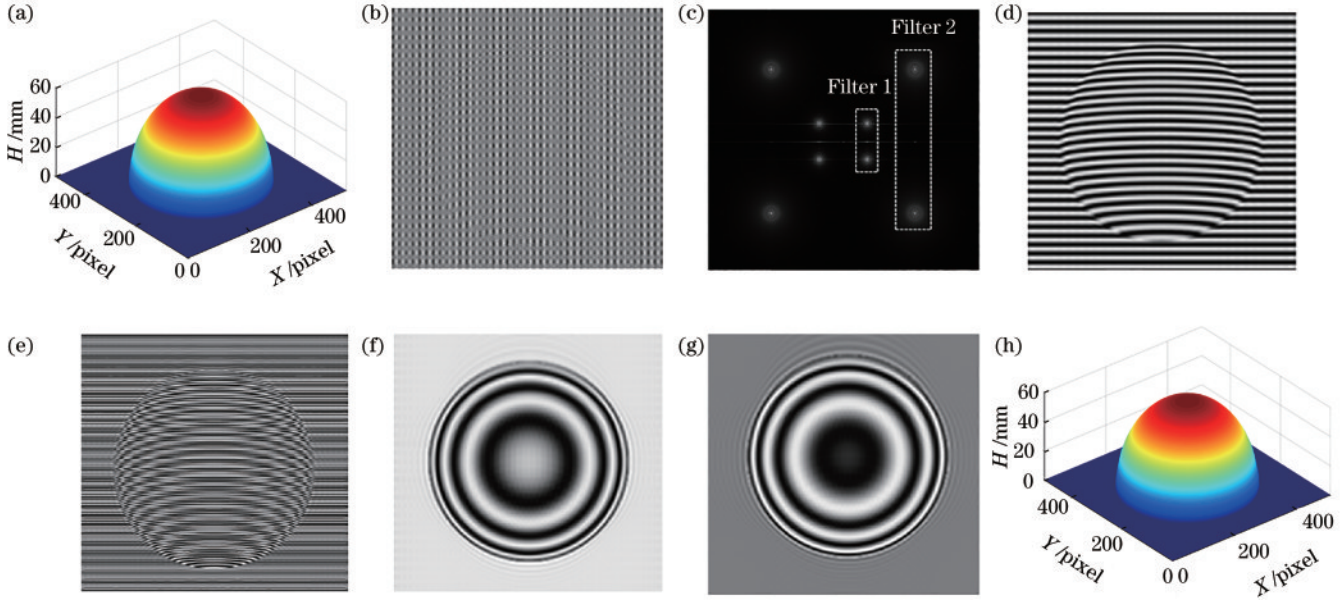

Fig. 3 Simulation of DFDM. (a) Measured object; (b) deformed composite fringe; (c) spectrum distribution; (d) low-frequency deformed fringe extracted via Filter 1; (e) high-frequency deformed fringe extracted via Filter 2; (f) extracted high-frequency Moiré fringe (sine); (g) extracted high-frequency Moiré fringe (cosine); (h) reconstructed result

ball" using DFDM is shown in Fig. 3(h), with a root mean square error (RMSE) of 0.0618 mm. To demonstrate the efficacy of digital π phase shift in DFDM, deformed fringe patterns with various frequencies are simulated, and the corresponding spectrum distribution is shown in Fig. 4(a1)-(d1). The AC and DC components of the fringe change from separate to aliasing as the frequency of the fringe decreases. The spectrum distribution after removing the DC component using digital π phase shift is shown in Fig. 4(a2)-(d2). Results show that digital digital π phase shift can effectively remove the DC component not only when the AC and DC are not aliased but also when they are.

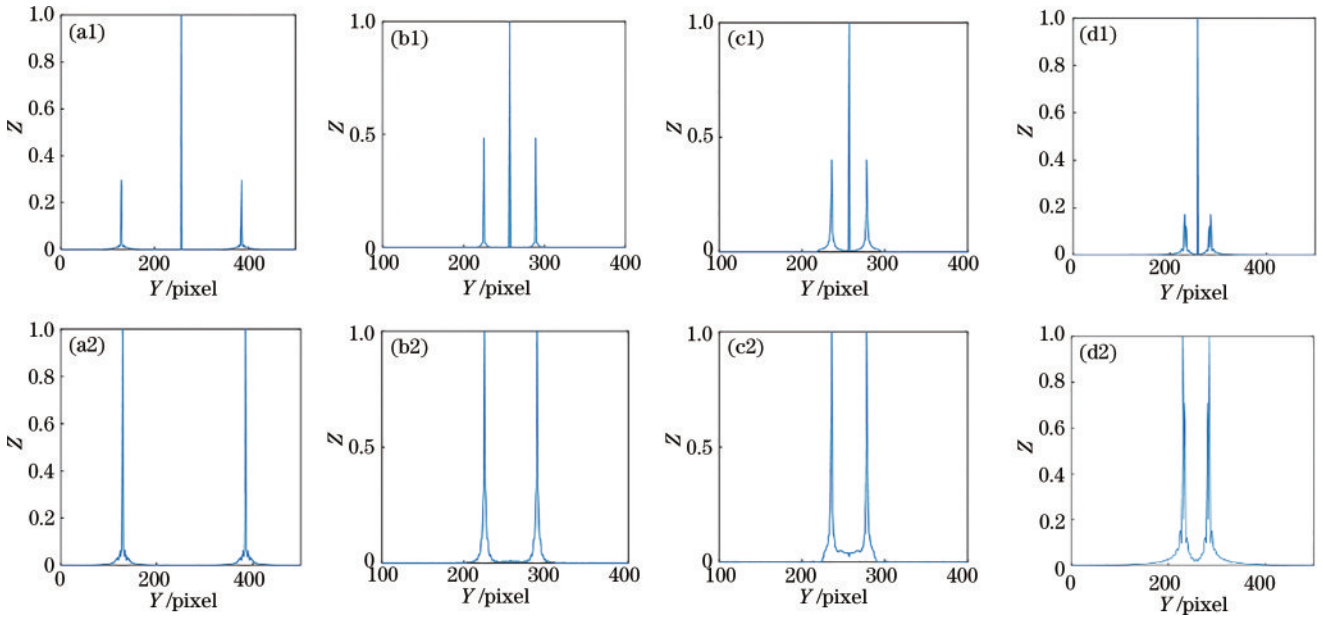

Fig. 4 Spectrum analysis. (a1)-(d1) Spectrum distribution of different frequency fringes; (a2)-(d2) spectrum distribution after removing the DC of Fig. 4 (a1)-(d1)

4 Experimental results and analysis

The 3D shapes of objects were measured. The composite fringe is generated via calculation according to the DFDM principle. The two modulation frequencies are $f_1 = 1/32$ pixel and $f_2 = 1/16$ pixel, respectively. The two carrier frequencies are $F_1 = 1/24$ pixel and $F_2 = 1/12$ pixel, respectively. The deformed composite fringe pattern collected using the camera MVC1000MF is shown in Fig. 5(a) after projecting the composite fringe onto the "face mask" by using the View Sonic PLED-W200 projector. Fig. 5(b) depicts the spectrum of a deformed composite fringe. Figs. 5(c) and 5(d) show the low- and high-frequency deformed fringes obtained using Filter 1 and Filter 2, respectively. In the frequency domain, the AC and DC components of low-frequency deformed fringes are more likely to overlap. Using digital π phase shift, the spectrum distribution after removing the DC component in Fig. 5(c) is shown in Fig. 5(e), which effectively removes the DC component. It is possible to extract the two high-frequency digital Moiré fringes shown in Figs. 5(f) and 5(g), which reflect the sine and cosine of phase only modulated by the "face mask" respectively. Fig. 5(h) is a reconstructed measured object. The outcome demonstrates that the "face mask" is accurately reconstructed and retains the majority of the surface detail.

The accuracy of DFDM and OMCGMP in measuring the same "face mask" is compared and analyzed experimentally. When the object is measured by OMCGMP, two fringes with the same frequency and π phase difference are orthogonally combined, and the two sinusoidal deformed fringes are subtracted to remove the DC component of sinusoidal fringes while retaining only the AC component. The frequency of the projection fringe is greater in the same experimental environment and equipment, and the reconstructed surface is finer. However, phase unwrapping may be incomplete. A lower frequency is usually chosen to correctly unwrap the phase, but the lower frequency is difficult to ensure accuracy. Thus, most details on the reconstructed 3D object surface are blurred. The high- and low-frequency fringes are combined in DFDM, and the temporal approach is used to unwrap the high-frequency wrapped phase, ensuring high object

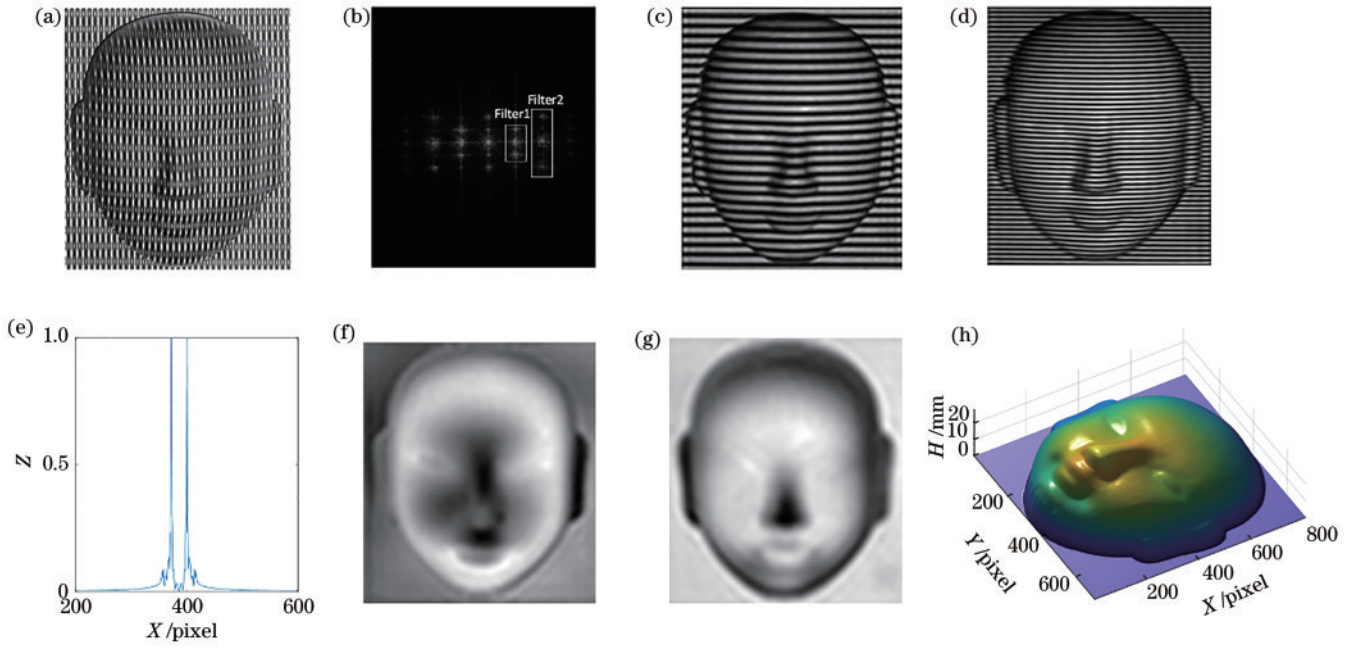

Fig. 5 Experiment of DFDM. (a) Deformed composite fringe; (b) spectrum distribution; (c) low-frequency deformed fringe extracted via Filter 1; (d) high-frequency deformed fringe extracted via Filter 2; (e) spectrum distribution of AC component in Fig. 6(c); (f) extracted high-frequency Moiré fringe (sine); (g) extracted high-frequency Moiré fringe (cosine); (h) reconstructed face mask

reconstruction accuracy. Figs. 6(a1) and (a2) are the low- and high-frequency deformed composite fringe obtained by OMCGMP, respectively. The deformed composite fringe pattern obtained by DFDM is shown in Fig. 6(b). Figs. 6(c1) and (c2) illustrate the reconstruction results using OMCGMP at low- and high-frequency, respectively. It can be seen that the low-frequency fringe measurement accuracy is low, and the high-frequency fringe phase unwrapping is incorrect. By contrast, the phase at high-frequency was unwrapped correctly using DFDM, as shown in Fig. 6(d). Table 1 compares the number of fringe patterns collected and measurement error by the two methods under the assumption of complete object contour reconstruction. It can be seen that DFDM only needs one reference fringe pattern, and it takes less time in the preparation

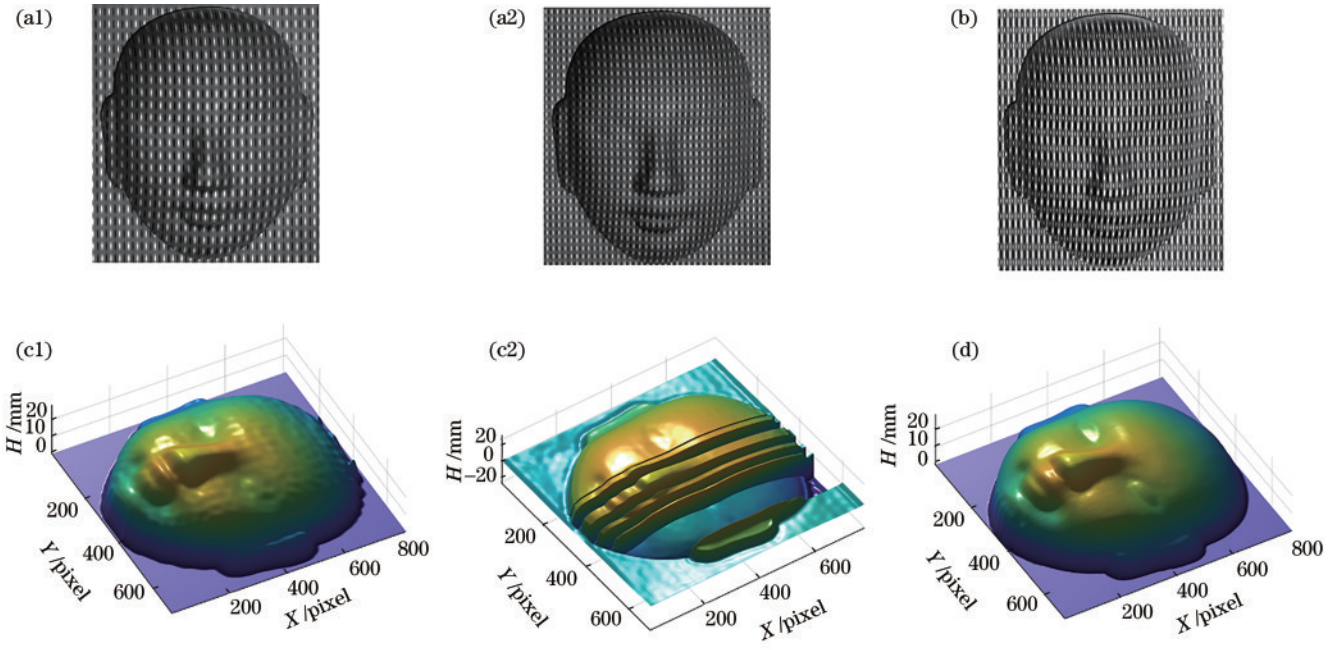

Fig. 6 Comparison of results obtained by OMCGMP and DFDM. (a1) Deformed pattern using OMCGMP at low-frequency; (a2) deformed pattern using OMCGMP at high-frequency; (b) deformed pattern using DFDM; (c1) reconstructed result using OMCGMP at low-frequency; (c2) reconstructed result using OMCGMP at high-frequency; (d) reconstructed result using DFDM

part. Taking the object reconstructed using the high-precision 16-PSP as the reference standard, the RMSE of the OMCGMP and DFDM is 0.1694 mm and 0.0737 mm, respectively. The cutaway views of the 240th row, 406th row, and 350th column of Figs. 6(c1) and 6(d), and the reconstruction result obtained by 16-PSP are shown in Fig. 7(a)-(c). The DFDM curve is significantly more similar to the 16-PSP curve than the OMCGMP curve. The outcome demonstrates that DFDM is more accurate than OMCGMP. At the same time, when compared with the 16-PSP, objects measured by DFDM require one deformed fringe to be captured, and the measurement speed is fast.

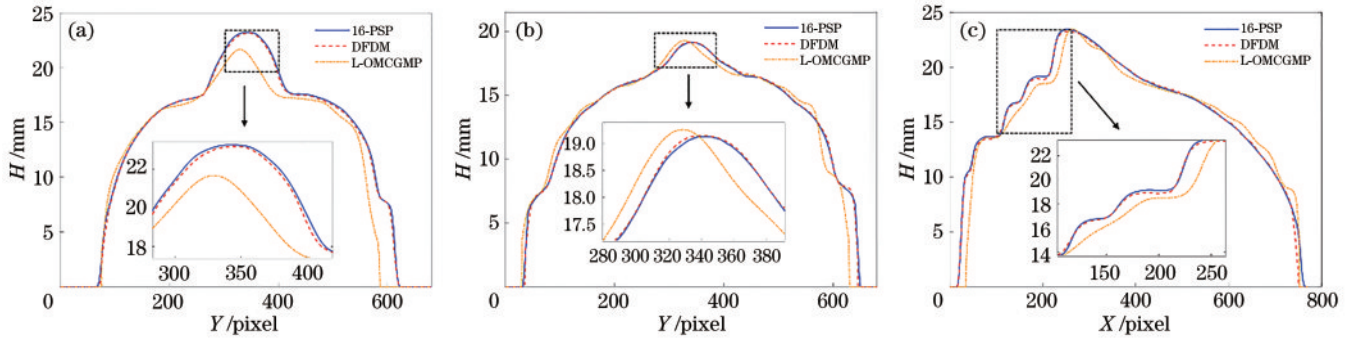

Fig. 7 Error analysis of results measured using OMCGMP and DFDM. (a) Cutaway view at line 240 with Figs. 6(c1) and 6(d), and the reconstructed result obtained by 16-PSP; (b) cutaway view at line 406 with Figs. 6(c1) and 6(d), and the reconstructed result obtained by 16-PSP; (c) cutaway view at column 350 with Figs. 6(c1) and 6(d), and the reconstructed result obtained by

Table 1 Experimental comparison results between OMCGMP and DFDM

Method	Reference fringe pattern	Deformed fringe pattern	RMSE /mm
OMCGMP	4	1	0.1694
DFDM	1	1	0.0737

Furthermore, space-isolated objects ("dolphin model" on the left and "fish model" on the right) are measured to validate the method's ability to measure discontinuous objects. Fig. 8(a) depicts the deformed fringe, whereas Fig. 8(b) depicts the reconstructed measured object. The results demonstrate that these models can be successfully reconstructed using DFDM. Similarly, using the object shape reconstructed via 16-PSP as a reference, the cutaway view at line 345 of the DFDM and 16-PSP space-isolated object reconstruction results is shown in Fig. 8(c). The similarity of the DFDM curve to the 16-PSP curve demonstrates the accuracy with which the 3D forms of several spatially independent objects are measured.

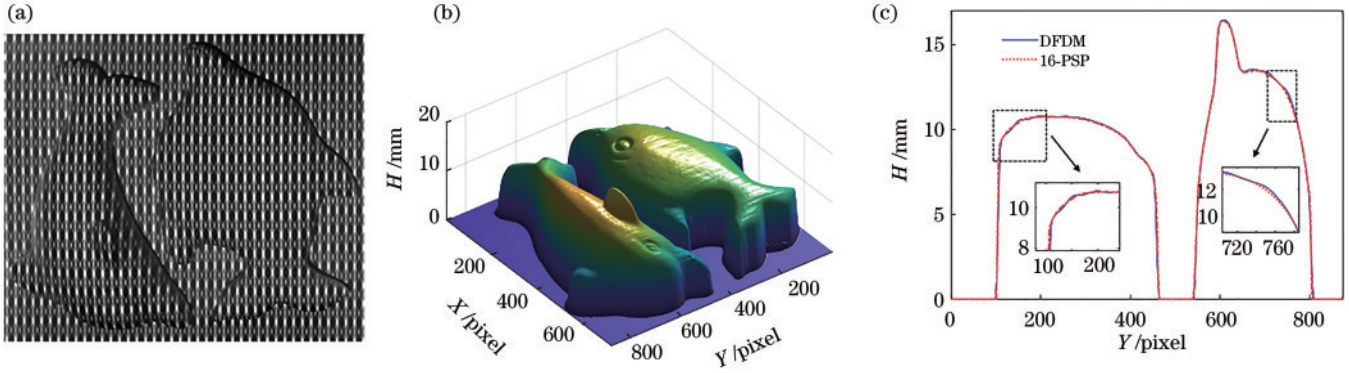

Fig. 8 Results of space-isolated objects reconstructed using DFDM. (a) Deformed composite pattern of space-isolated objects; (b) reconstructed result of Fig. 8(a); (c) cutaway view at line 345 with Fig. 8 (b) and the reconstructed result obtained by 16-PSP

5 Conclusions

The DFDM is proposed for 3D object shape measurement. Digital π phase shift is used to remove the DC component of the fringe. Whether the AC or DC components of the fringe are aliased, the DC component can be removed well, ensuring Moiré fringe accuracy. At the same time, dual-frequency Moiré fringes can be used to obtain the phase more precisely, improving the object's measurement accuracy. The RMSE of DFDM is 0.0618 mm, according to the results of the simulated reconstruction of the "crown

ball." In the experiment, the measurement of the "face mask" is carried out. The result shows that the RMSE of high-accuracy DFDM is only 0.0737 mm, which is significantly less than the RMSE of OMCGMP, with 0.1694 mm. Simultaneously, DFDM is used to assess the "dolphin model" and "fish model". The measurement results are remarkably similar to those obtained using 16-PSP, demonstrating the efficacy of DFDM even more. DFDM reconstructs objects with only one deformed fringe, which has broader application prospects in the field of real-time 3D shape measurement.

References

[1] Yang S C, Huang H L, Wu G X, et al. High-speed three-dimensional shape measurement with inner shifting-phase fringe projection profilometry[J]. Chinese Optics Letters, 2022, 20(11): 112601.

[2] Yan F, Qi J, Liu Y P, et al. Three-dimensional measurement method of binary coded fringe focusing projection[J]. Acta Optica Sinica, 2022, 42(22): 2212002.

[3] Zhang J L, Guo W B, Wu Z J, et al. 3D shape measurement using speckle-embedded fringes and lookup table[J]. Acta Optica Sinica, 2021, 41(5): 0512003.

[4] Liu L, Xi D D, Chen Z J, et al. Three-dimensional shape measurement based on hybrid dual-frequency fringe projection[J]. Laser & Optoelectronics Progress, 2021, 58(12): 1212001.

[5] Feng S J, Zuo C, Tao T Y, et al. Robust dynamic 3-D measurements with motion-compensated phase-shifting profilometry[J]. Optics and Lasers in Engineering, 2018, 103: 127-138.

[6] Guo Q H, Ruan Y X, Xi J T, et al. 3D shape measurement of moving object with FFT-based spatial matching[J]. Optics & Laser Technology, 2018, 100: 325-331.

[7] Peng K, Cao Y P, Wu Y C, et al. A new method using orthogonal two-frequency grating in online 3D measurement [J]. Optics & Laser Technology, 2016, 83: 81-88.

[8] Zhong K, Li Z W, Li R F, et al. Pre-calibration-free 3D shape measurement method based on fringe projection[J]. Optics Express, 2016, 24(13): 14196-14207.

[9] Li B W, An Y T, Zhang S. Single-shot absolute 3D shape measurement with Fourier transform profilometry [J]. Applied Optics, 2016, 55(19): 5219-5225.

[10] Song K C, Hu S P, Wen X, et al. Fast 3D shape measurement using Fourier transform profilometry without phase unwrapping[J]. Optics and Lasers in Engineering, 2016, 84: 74-81.

[11] Su X Y, Chen W J. Fourier transform profilometry: a review[J]. Optics and Lasers in Engineering, 2001, 35 (5): 263-284.

[12] Takeda M, Mutoh K. Fourier transform profilometry for the automatic measurement of 3-D object shapes[J]. Applied Optics, 1983, 22(24): 3977-3982.

[13] Li D L, Cao Y P, Fu G K, et al. An improved 2+1 phase-shifting algorithm[J]. Optics Communications, 2019, 444: 165-171.

[14] Flores J L, Ferrari J A, Torales G G, et al. Color-fringe pattern profilometry using a generalized phase-shifting algorithm[J]. Applied Optics, 2015, 54(30): 8827-8834.

[15] Pan J H, Huang P S, Chiang F P. Color phase-shifting technique for three-dimensional shape measurement[J]. Optical Engineering, 2006, 45(1): 013602.

[16] Liu W Y, Wang Z Q, Mu G G, et al. Color-coded projection grating method for shape measurement with a single exposure[J]. Applied Optics, 2000, 39(20): 3504-3508.

[17] Wang Z Y, Zhang Z H, Gao N, et al. Single-shot 3D shape measurement of discontinuous objects based on a coaxial fringe projection system[J]. Applied Optics, 2019, 58(5): A169-A178.

[18] He Y H, Cao Y P. Three-dimensional measurement method with orthogonal composite grating aided by fringe contrast and background calibration[J]. Optical Engineering, 2010, 49(7): 073603.

[19] Guo H Y, Zhou H W, Banerjee P. Single-shot digital phase-shifting Moiré patterns for 3D topography[J]. Applied Optics, 2021, 60(4): A84-A92.

[20] Zhu Y B, Wen H H, Zhang H Y, et al. Application of digital phase shifting Moiré method in interface and dislocation location recognition and real strain characterization from HRTEM images[J]. Optics Express, 2019, 27(25): 36990-37002.

[21] Wang S Y, Yan K D, Xue L. High speed Moire based phase retrieval method for quantitative phase imaging of thin objects without phase unwrapping or aberration compensation[J]. Optics Communications, 2016, 359: 272-278.

[22] Li C M, Cao Y P, Chen C, et al. Computer-generated Moiré profilometry[J]. Optics Express, 2017, 25(22): 26815-26824.

[23] Wang L, Cao Y P, Li C M, et al. Orthogonal modulated computer-generated Moiré profilometry[J]. Optics Communications, 2020, 455: 124565.

[24] An H H, Cao Y P, Li H M, et al. An accuracy improving method for composite grating phase measuring profilometry[J]. Optics Communications, 2020, 477: 126343.

[25] Yang F J, Dai M L, He X Y, et al. Single fringe projection profilometry based on sinusoidal intensity normalization and subpixel fitting[J]. Optics and Lasers in Engineering, 2011, 49(3): 465-472.

[26] Fu Y J, Jiang G Y, Chen F Y. A novel Fourier transform profilometry based on dual-frequency grating [J]. Optik, 2012, 123(10): 863-869.

[27] Kinell L. Spatiotemporal approach for real-time absolute shape measurements by use of projected fringes[J]. Applied Optics, 2004, 43(15): 3018-3027.

[28] Ma Q N, Cao Y P, Chen C, et al. Intrinsic feature revelation of phase-to-height mapping in phase measuring profilometry[J]. Optics & Laser Technology, 2018, 108: 46-52.